Available online at www.sciencedirect.com
SCIENCE DIRECT®
Journal of volcanology and geothermal research
Journal of Volcanology and Geothermal Research 154 (2006) 63–73
www.elsevier.com/locate/jvolgeores

Bulk and particle strain analysis in high-temperature deformation experiments

Steven L. Quane [a,*], J.K. Russell [b]

[a] 7750 Sunshine Canyon Dr. Boulder, CO 80302, United States
[b] Volcanology & Petrology Laboratory, Department of Earth & Ocean Sciences, University of British Columbia, 6339 Stores Rd., Vancouver, B.C., Canada V6T 1Z4

Received 1 December 2004; accepted 30 September 2005
Available online 24 February 2006

Abstract

Experimental data alone are not sufficient to describe the rheology of deformed geomaterials. To fully characterize a material's rheological properties, independent verification of deformation mechanisms is required. Here, we use standard image analysis techniques to semi-quantify the physical changes in experimentally deformed cores of soda-lime silica glass beads and rhyolite ash previously described by Quane and Russell [Quane, S.L., Russell, J.K., 2005a. Welding: insights from high-temperature analogue experiments. J. Volcanol. Geotherm. Res. 142, 67–87]. The properties we measure by image analysis include porosity, radial bulging and particle elongation. The image analysis measurements combined with digital output from the experiments allow us to determine the amount of total axial and radial strain accumulated by the bulk sample (ε_b) and by individual particles (ε_p). We demonstrate that these metrics of strain are nearly equal to the one-dimensional strain recorded by the deformation apparatus (ε_m) and sample shortening (ε_s), confirming that all strain introduced by the deformation apparatus is being transferred into both the bulk sample and individual particles. We also show that ε_b is manifest as two discrete components: axial (ε_a) and radial (ε_r) strain. We use these independent components of strain accumulation to show that, despite having nearly identical strain–time and stress–strain deformation paths, glass bead cores and rhyolite ash cores have strikingly different mechanisms of strain accumulation. In the higher porosity rhyolite ash cores, axial strain dominates, implying that, under the conditions present, natural glassy particulate geomaterials deform almost entirely by porosity loss.

Keywords: image analysis; strain; welding; experimental; rheology

1. Introduction

Rock deformation presses provide an effective means of studying deformation processes at geologically relevant conditions and have been developed in support of crustal (e.g., Tullis and Tullis, 1986; Rutter, 1993; Austin et al., 2005), mantle (e.g., Karato et al., 1998) and volcanological (Bagdassarov et al., 1996; Dingwell, 1998; Spieler et al., 2003; Quane et al., 2004) studies. These experiments provide two separate but complementary types of information. Firstly, the output of each experiment (i.e., time, load and strain) indirectly shows the rheological properties of the material. These results constrain constitutive relationships used to model natural deformational processes (e.g., strain) as a function of environmental (e.g., temperature, pressure) and material (e.g., viscosity) properties. A second, and equally important,

* Corresponding author.
E-mail address: squane@eos.ubc.ca (S.L. Quane).

0377-0273/$ - see front matter © 2006 Elsevier B.V. All rights reserved.
doi:10.1016/j.jvolgeores.2005.09.025

source of information derives from the experimental run products themselves. The run products make available a plethora of textural and structural data that provide macro- to microscopic verification of the styles of deformation (e.g., viscous vs. brittle). Furthermore, the run products allow for additional measurements such as porosity and particle elongation which provide additional constraints on the rheology of experimental materials.

In this paper, we review a series of high-temperature deformation experiments on cores of sintered soda-lime silica glass beads and rhyolitic ash which were used as analogues for welding of pyroclastic deposits (Quane et al., 2004; Quane and Russell, 2005a). Specifically, we demonstrate the contribution that image analysis measurements can make in fully characterizing experimental end products by re-analyzing results from Quane and Russell (2005a) using new and more accurate image analysis techniques. The techniques employed here and differences between this study and Quane and Russell (2005a) are described in a later section.

The image analysis measurements on the experimental run products are used to:

(a) demonstrate coincidence between instrumental or experimental one-dimensional strain and the axial and radial strain recorded by the sample, indicating that strain is not being partitioned into the deformation apparatus,
(b) show that axial and radial strain are homogeneously distributed across the core and particles and that there is little to no strain localization,
(c) quantify porosity in experimental run products and, thus, provide an independent check on the magnitude of volume strain occurring during the experiment,
(d) demonstrate that deformation is purely coaxial throughout the experiment and
(e) provide an independent means by which to interpret the nature and type of strain (e.g., volumetric vs. pure shear) accommodated by experimentally deformed samples.

Lastly, we compare results of deformation experiments on cores of soda-lime silica glass beads to similar experiments performed on cores of rhyolitic ash (Quane and Russell, 2005a). The glass bead cores comprise solid, spherical particles and feature relatively low initial bulk porosities ($\phi_o = \sim 30\%$). In contrast, the cores of sintered rhyolite ash are made of porous, irregularly shaped particles and have substantially higher initial bulk porosities ($\phi_o = \sim 73\%$). Despite the striking similarity in the digital data (e.g., experimental response) recovered from the experiments, textural data show that the two materials record substantially different deformation paths.

1.1. Volcanological deformation experiments

High-*T* deformation experiments have become important and widespread tools of investigation in the volcanological sciences. Such experiments supply data pertinent to the formation and collapse of lava flows and domes (e.g., Spieler et al., 2003), the transport and fragmentation of magma in conduits (e.g., Spieler et al., 2004; Tuffen and Dingwell, 2005), and the high-*T* rheology of pyroclastic material (e.g., Boyd, 1961; Friedman et al., 1963; Yagi, 1966; Bierwirth, 1982; Quane et al., 2004; Grunder et al., 2004; Quane and Russell, 2005a). Quane et al. (2004) described a deformation apparatus designed for high-*T*, unconfined, low-load (<1136 kg) deformation experiments on volcanological materials (Volcanology Deformation Rig, VDR). The VDR is used to run controlled, constant displacement rate or constant load experiments at fixed temperatures. One of the main attributes of the VDR is that it accommodates samples that are up to 7.5 cm in diameter and 10 cm long. This size allows for extensive post-experimental analysis. A large portion of this post-experimental analysis of run products involves analysis of digital images of cores and thin sections made perpendicular to the direction of loading.

Below, we examine strain accumulation in end products from thirty-two high-temperature deformation experiments performed on cores of sintered soda-lime silica glass beads (Quane and Russell, 2005a; Table 1). We also compare these results with seven experiments performed on cores of sintered rhyolite ash (Quane, 2004). The experiments elucidate the mechanisms, rheology and time-scales of welding in natural pyroclastic deposits (Quane et al., 2004; Quane and Russell, 2005a,b). Welding in pyroclastic deposits results from the sintering, compaction and flattening of pyroclasts held at or above their glass transition temperature for times longer than the relaxation time-scales of the silicate melts (e.g., Smith, 1960; Ross and Smith, 1961; Guest and Rogers, 1967; Sparks and Wright, 1979; Giordano et al., 2005). The high-temperature experiments used both constant displacement rate and constant load constraints (Quane, 2004; Quane et al., 2004; Quane and Russell, 2005a). Displacement rates varied from 2.5×10^{-5} cm/s to 1×10^{-3} cm/s; loads ranged from ~5 to 100 kg ($\sigma = 0.03$ to ~0.65 MPa). Isothermal experiments were performed at 535, 550, 600 and 650 °C for soda-lime silica glass beads and 850 °C for Rattlesnake Tuff

Table 1
Summary of conditions of high-temperature deformation experiments performed on cores of soda-lime silica glass beads and properties of run products

Experiment	T (°C)	Rate (cm/s)	σ (MPa)	ΔL	ε_m	ε_s	ϕ_o	ϕ_f	ε_a	r_f	ε_r	ε_b	ε_p	1s
sq_06_24a	600	2.5E−04	*	4.000	0.61	0.58	0.36	1.10	0.29	2.62	0.28	0.58	0.50	0.09
sq_06_24b	600	1.0E−03	*	4.575	0.62	0.67	0.34	0.06	0.30	2.66	0.31	0.60	0.60	0.08
sq_06_25a	600	5.0E−04	*	3.920	0.63	0.58	0.34	0.09	0.28	2.70	0.32	0.60	0.50	0.08
sq_06_25b	550	5.0E−04	*	3.800	0.61	0.55	0.39	0.21	0.24	2.80	0.37	0.61	–	–
sq_06_27a	600	5.0E−04	*	4.550	0.61	0.62	0.32	0.05	0.29	2.70	0.33	0.61	0.57	0.08
sq_07_04a	600	5.0E−04	*	4.200	0.63	0.58	0.32	0.06	0.28	2.63	0.29	0.56	0.55	0.07
sq_07_04b	600	2.5E−04	*	4.085	0.63	0.58	0.32	0.05	0.28	2.65	0.30	0.58	0.57	0.07
sq_07_16a	650	5.0E−04	*	4.075	0.54	0.55	0.29	0.04	0.26	2.71	0.33	0.59	0.58	0.07
sq_07_16b	550	5.0E−04	*	3.520	0.50	0.48	0.37	0.14	0.26	2.63	0.29	0.55	–	–
sq_07_17a	600	5.0E−04	*	2.625	0.36	0.35	0.31	0.12	0.22	2.34	0.10	0.32	0.33	0.10
sq_07_17b	600	1.0E−03	*	3.910	0.52	0.54	0.35	0.09	0.29	2.68	0.31	0.61	0.51	0.07
sq_07_18a	600	*	0.060	3.050	0.42	0.42	0.31	0.13	0.21	2.49	0.21	0.41	0.44	0.08
sq_07_18b	600	*	0.050	2.900	0.37	0.38	0.33	0.15	0.21	2.50	0.21	0.42	0.37	0.09
sq_07_19a	600	*	0.045	2.000	0.31	0.28	0.31	0.16	0.18	2.31	0.07	0.26	0.31	0.10
sq_07_22a	600	*	0.037	1.800	0.26	0.25	0.34	0.19	0.18	2.28	0.05	0.23	0.26	0.08
sq_07_22b	600	*	0.031	1.630	0.21	0.21	0.34	0.19	0.18	2.22	0.00	0.18	0.23	0.09
sq_07_22c	600	*	0.024	1.200	0.16	0.15	0.33	0.30	0.05	2.36	–	0.17	0.17	0.09
sq_07_23a	600	*	0.026	0.900	0.10	0.10	0.34	0.31	0.05	2.26	0.03	0.08	0.12	0.09
sq_07_23b	600	*	0.033	3.100	0.36	0.40	0.38	0.17	0.26	2.40	0.14	0.40	0.37	0.09
sq_07_24a	600	5.0E−04	*	4.300	0.52	0.61	0.31	0.14	0.19	2.96	–	0.63	0.56	0.09
sq_07_24b	600	*	0.058	4.375	0.59	0.63	0.32	0.09	0.25	2.79	0.37	0.62	0.57	0.10
sq_07_28a	550	*	0.170	2.850	0.40	0.41	0.38	0.16	0.27	2.49	0.21	0.48	0.40	0.10
sq_08_04a	600	*	0.015	2.950	0.37	0.40	0.32	0.11	0.24	2.38	0.13	0.37	–	–
sq_08_06a	550	*	0.111	1.900	0.29	0.29	0.30	0.15	0.18	2.31	0.08	0.26	0.35	0.11
sq_08_06b	550	*	0.035	1.610	0.16	0.22	0.36	0.29	0.10	2.32	0.09	0.18	0.22	0.12
sq_08_07b	535	*	0.161	1.775	0.27	0.27	0.35	0.23	0.15	2.37	0.12	0.27	0.31	0.10
sq_08_08a	535	*	0.322	2.725	0.40	0.41	0.37	0.21	0.20	2.56	0.25	0.45	0.40	0.10
sq_08_08b	535	*	0.036	1.150	0.17	0.18	0.37	0.29	0.11	2.23	0.01	0.12	0.17	0.12
sq_08_09a	535	*	0.160	1.925	0.28	0.28	0.34	0.23	0.15	2.43	0.17	0.32	0.28	0.08
sq_08_11a	535	*	0.160	2.250	0.33	0.33	0.31	0.17	0.17	2.46	0.19	0.35	0.39	0.11
sq_08_11b	600	5.0E−04	*	3.600	0.52	0.49	0.29	0.10	0.21	2.61	0.28	0.49	0.50	0.11
sq_08_12a	600	5.0E−04	*	3.700	0.48	0.53	0.30	0.07	0.25	2.54	0.24	0.49	1.48	0.11
sq_08_04b	600	*	*	*	*	*	0.29	0.29	*	2.22	*	*	*	*
Rattlesnake Tuff samples														
sq_08_24a	850	1.25E−04	*	2.307	0.48	0.46	0.75	0.62	0.34	2.09	0.17	0.51	*	*
sq_08_25a	850	5.00E−04	*	2.444	0.38	0.47	0.73	0.61	0.31	2.18	0.23	0.54	*	*
sq_01_13a	850	5.00E−04	*	3.055	0.69	0.61	0.73	0.44	0.52	2.11	0.19	0.71	*	*
sq_08_26b	850	*	0.28	1.825	0.27	0.34	0.75	0.70	0.15	2.15	0.22	0.36	*	*
sq_01_14a	850	*	0.64	1.999	0.41	0.38	0.72	0.65	0.20	2.16	0.22	0.43	*	*
sq_01_14b	850	*	0.64	2.669	0.53	0.50	0.73	0.59	0.35	2.17	0.23	0.58	*	*
sq_01_15a	850	*	0.33	1.704	0.35	0.32	0.73	0.68	0.15	2.13	0.20	0.35	*	*

Parameters include: shortening (ΔL), machine strain (ε_m), sample strain (ε_s) initial porosity (ϕ_o), final porosity (ϕ_f), radial strain (ε_a) final radius (r_f), radial strain (ε_r), bulk strain (ε_b) and particle strain (ε_p). 1s is calculated standard deviation on ε_p based on measurement uncertainty on c/a values. '–' Denotes sample damaged before measurement.
Experiments use constant displacement rate (dL/dt) or constant load (e.g., stress, σ).

rhyolite ash. At these temperatures the melt viscosities of the two materials are in the range of 10^7 to 10^9 Pa s and within one order of magnitude (Quane, 2004).

1.2. Rheological data

The types of output we recover from both constant load and constant displacement rate experiments are summarized in Fig. 1. During constant load deformation experiments (i.e., welding), strain accumulates non-linearly with time (Fig. 1). As expected, higher deformation rates and higher imposed loads lead to higher total strains for a given amount of time (Fig. 1). Photomicrographs of deformed experimental end products indicate no evidence for brittle deformation (e.g., microcracks, Fig. 2b, c, d). It should be noted here that

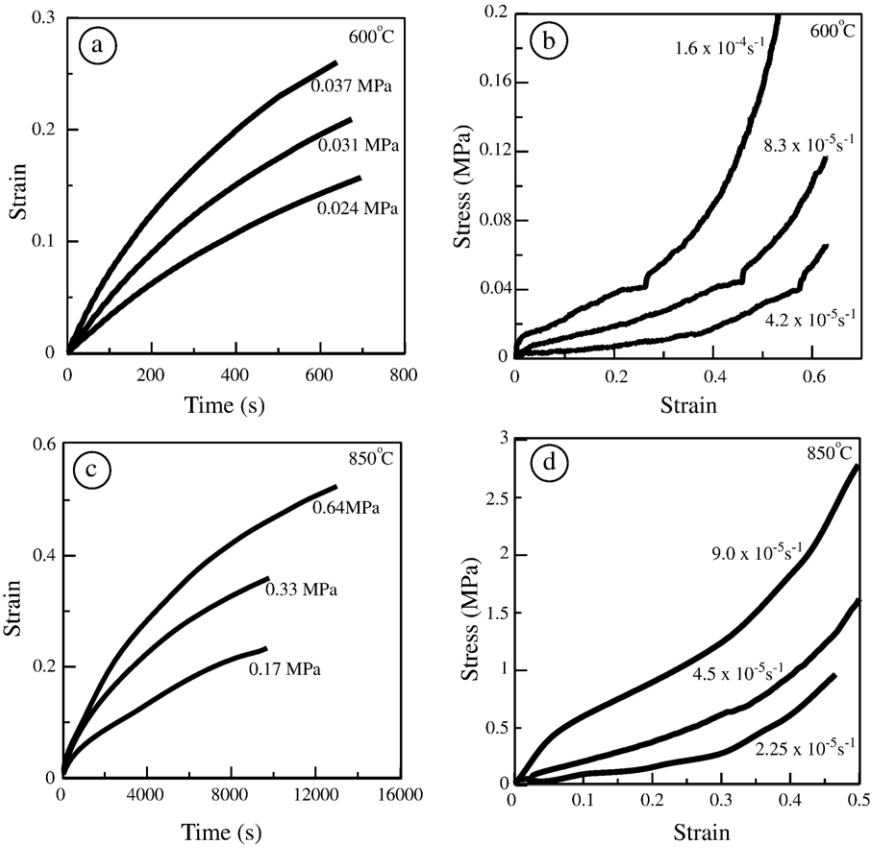

Fig. 1. Representative results from high-temperature deformation experiments on cores of sintered soda-lime silica glass beads (Quane and Russell, 2005a) and Rattlesnake Tuff ash (Quane, 2004). a) Data from experiments performed at 600 °C and under constant loads corresponding to load stresses of 0.037, 0.031 and 0.024 MPa on cores of glass beads plotted as values of strain versus time (s). Cumulative strain increases with time and load stress. b) Data from experiments performed at 600 °C under constant displacement rates corresponding to strain rates of 1.6×10^{-4}, 8.3×10^{-5} and $4.2\times10^{-5}\,s^{-1}$ on cores of glass beads plotted as strain versus stress. c) Data from experiments performed at 850 °C and under constant loads corresponding to load stresses of 0.64, 0.33, 0.17 MPa on cores of Rattlesnake Tuff ash. d) Data from experiments performed at 850 °C under constant displacement rates corresponding to strain rates of 9.0×10^{-5}, 4.5×10^{-5} and $2.25\times10^{-5}\,s^{-1}$ on cores of Rattlesnake Tuff ash.

the microcracks in the undeformed sample (Fig. 2a) are formed either during rapid cooling of the material or in the making of the thin section and are not due to deformational processes. Our hypothesis is that the sample is deforming entirely by viscous processes. The stiffening, or strain hardening by viscosity increase (Fig. 1), is occurring due to porosity reduction (e.g., Ducamp and Raj, 1989; Sura and Panda, 1990; Quane and Russell, 2005a; Russell and Quane, 2005). These experiments produce results which speak directly to the mechanisms, rheology and time-scales of welding processes in volcanology. However, to uniquely define the rheology of these materials and to determine how strain accumulates during deformation requires data that are best obtained from image analysis measurements on the run products.

The ability to perform post-experiment analysis on the run products represents a substantial improvement over previous high-temperature deformation studies. For example, strain–time paths for constant load experiments run by Friedman et al. (1963) and Bierwirth (1982) are very similar to our data (Fig. 1). However, Friedman et al. (1963) and Bierwirth (1982) did not have the opportunity to examine their run products and, therefore, had to assume that all strain recorded by their experimental device was passed on to the sample via viscous deformation. These conclusions, while seemingly correct, need independent verification. For example, experiments controlled by other styles of deformation can generate identical strain–time paths. Constant load experiments simulating low-temperature compaction creep in quartz sand (e.g., He et al., 2003; Karner et al., 2003; Chester et al., 2004) showed very similar patterns to those shown in Fig. 1. However, visual analysis of their experimental end products showed pervasive brittle deformation (i.e., cracking)

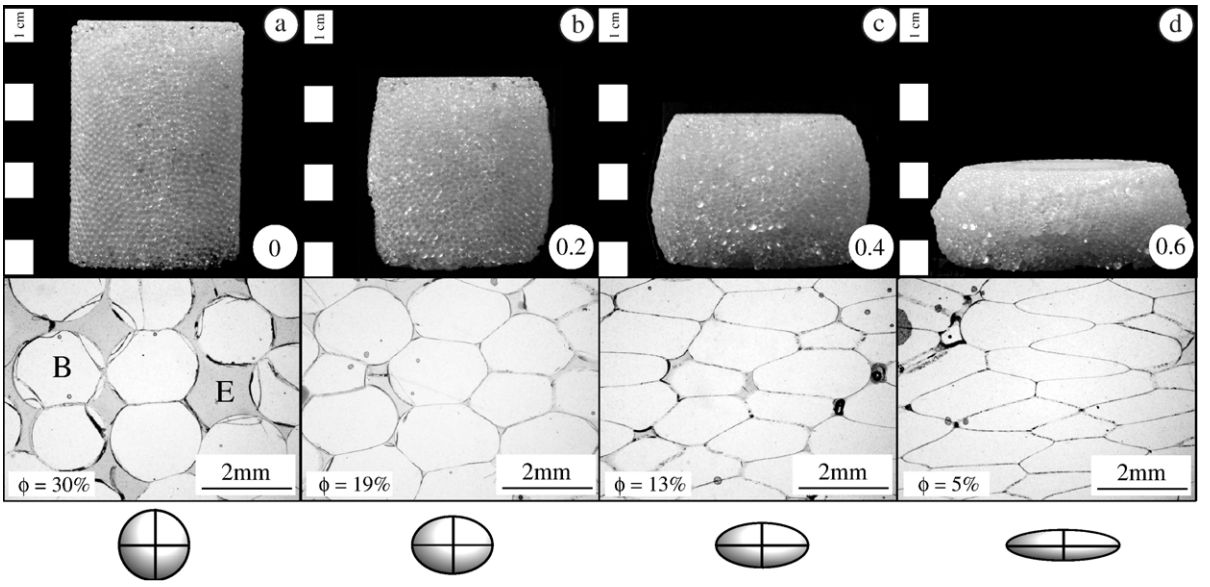

Fig. 2. Representative samples of starting materials and run products for experiments on cores of glass beads shown as photographs (top) and photomicrographs of corresponding thin sections (bottom): a) core of sintered and undeformed glass beads. (B) Having an initial porosity (ϕ_o) of ≈30% defined by colored epoxy (E). Note, microcracks are a result of either quenching or thin sectioning and do not represent brittle deformation. Also shown are run products resulting from higher amounts of strain: b) 0.2 (ϕ_f=19%), c) 0.4 (ϕ_f=13%), and d) 0.6 (ϕ_f=5%).

affecting individual quartz grains (e.g., Chester et al., 2004) confirming their hypothesis that brittle mechanical processes such as grain crushing contribute to porosity reduction in buried sands.

2. Methodology

Our intent is to use image analysis measurements to recover additional information from experimentally deformed cores of sintered soda-lime silica glass beads previously described by Quane and Russell (2005a). The glass bead core experiments have several important attributes which aid post-experiment analysis. Firstly, the samples are ~4.4 cm in diameter and ~6 cm in length and comprise uniform-sized beads (e.g., 2 mm beads; Fig. 2). The large sample to particle size ratio ensures significant numbers of individual particles for post-experiment analysis. Secondly, the starting materials are well characterized and individual beads have known and constant physical properties (e.g., density, temperature dependent viscosity). Thirdly, the beads are spherical in shape having a maximum variation in sphericity of 10%. The run products were characterized by Quane and Russell (2005a) by measuring initial porosity (ϕ_o), final porosity (ϕ_f), initial radius (r_o), final radius (r_f), sample displacement (ΔL), and individual glass bead particle elongation. Here we expand and improve on the image analysis techniques they used and investigate relationships between bulk, sample and particle strain that were not explored by Quane and Russell (2005a).

The major difference between this study and Quane and Russell (2005a) is the use of Scion® image analysis software to measure geometrical properties of the experimental cores. After each experiment, digital photos of each end product were taken (e.g., Fig. 2). All photos were taken at the same scale (i.e., focal length was identical). In addition, a digital photograph of an object of known dimensions (ruler) was taken under exactly the same conditions. Using this information, we were able to scale all photographs in Scion® image analysis software and accurately determine final core geometries. This procedure was a significant improvement over that of Quane and Russell (2005a) because we were able to eliminate difficult and inaccurate caliper measurements on deformed experimental end products.

The initial porosity (ϕ_o; Table 1) is determined from density measurements on each core:

$$\phi_o - \frac{\rho_m - \rho_T}{\rho_m} \quad (1)$$

where ρ_m is the density of the framework material (glass beads=2.49 g/cm^3) and ρ_T is the density of the starting material based on measurements of core mass and volume. Volumes are determined by measurements of core geometries (length and radius). Quane and Russell (2005a) determined these properties using

multiple digital caliper measurements of length and diameter of the cores. In this study, we also determine the initial length of each core using multiple digital caliper measurements; however, we determined initial core radius using Scion® image analysis measurements on a scaled photograph of starting material (sq_08_04b; Fig. 2) to determine a representative starting material radius. The new value is 2.23 as opposed to 2.2 from caliper measurements (Quane and Russell, 2005a).

The final porosity (ϕ_f; Table 1) of the run product is estimated via image analysis measurements (Fig. 3). After each experiment, samples were impregnated with blue epoxy and thin sectioned. The blue epoxy provided a stark contrast between the void space and glass beads (Fig. 3b). We exploited this contrast to measure final porosity using Scion® image analysis software on digital scans of each thin section (Fig. 3). Final porosity was determined as the proportion of void (or colored) space relative to the entire area of the thin section (Fig. 3c and d). A more color-sensitive filter was employed in this study rendering more accurate results for ϕ_f relative to those of Quane and Russell (2005a).

We determine ΔL by taking the difference between pre- and post-experiment sample length (e.g., Quane and Russell, 2005a). As discussed above, initial length values were measured using digital calipers. However, in this study we used Scion® image analysis software on scaled photos of each experimental end product to determine final sample length, thus eliminating caliper measurements on the deformed cores and rendering more accurate values for ΔL.

Final core radii were also determined using a new technique. The experimental cores bulge during experiment (e.g., Fig. 2). Therefore, it is very difficult to determine the average radius of the experimental end product on the curved core surface using digital calipers. Therefore, we improved on the method of Quane and Russell (2005a) by employing image analysis to measure final core radii. Specifically, the two-dimensional area was determined for all deformed end products by analyzing scaled digital photographs using Scion® image analysis software (Fig. 3a; Table 1). Average final radii (r_f) were calculated using these values, measured values for final core length and the geometric relationship for the area of a rectangle.

Glass bead particle elongation estimates are made by analyzing images of thin sections of run products cut perpendicular to the loading direction (Fig. 4). To determine the axial (c) and radial (a) dimensions of individual beads we made several images of each thin section using a standard microfiche reader. We then hand-traced bead outlines (~500 for 2 mm bead section and ~1000 for 1 mm bead sections; Fig. 4). Traces were scanned and individual grains were fitted to model ellipses using Scion® image analysis software (Fig. 4c

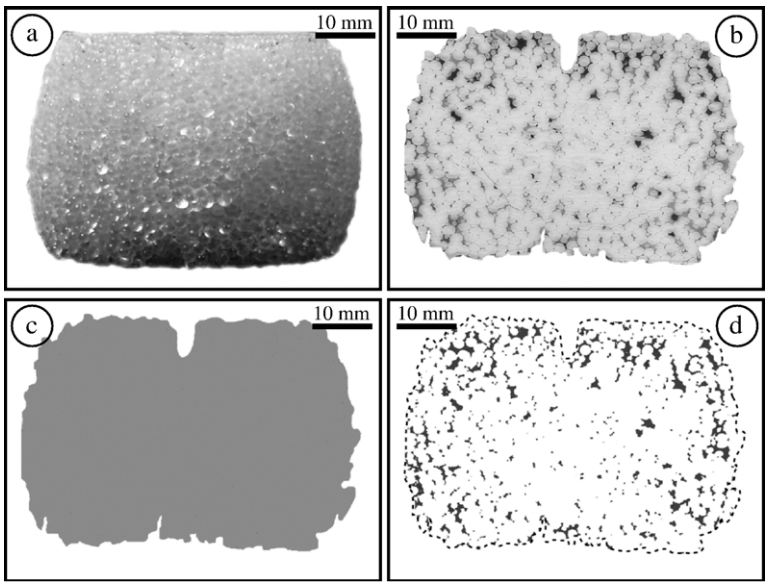

Fig. 3. Summary of image analysis methods used to estimate sample porosity on experimental run products. a) Photograph of sample core at the end of high-temperature deformation experiment. b) Image of thin section of sample core created using standard flatbed scanner (scanned at 600 dpi resolution); porosity is illustrated by colored dark gray epoxy. c) Gray-shaded image of thin section image shown in (b) is used to quantify the total area of thin-section. d) Processed image of entire thin section (dotted line) which identifies and separates the pore space (dark) from the deformed glass beads (light) used to estimate the total porosity of the sample.

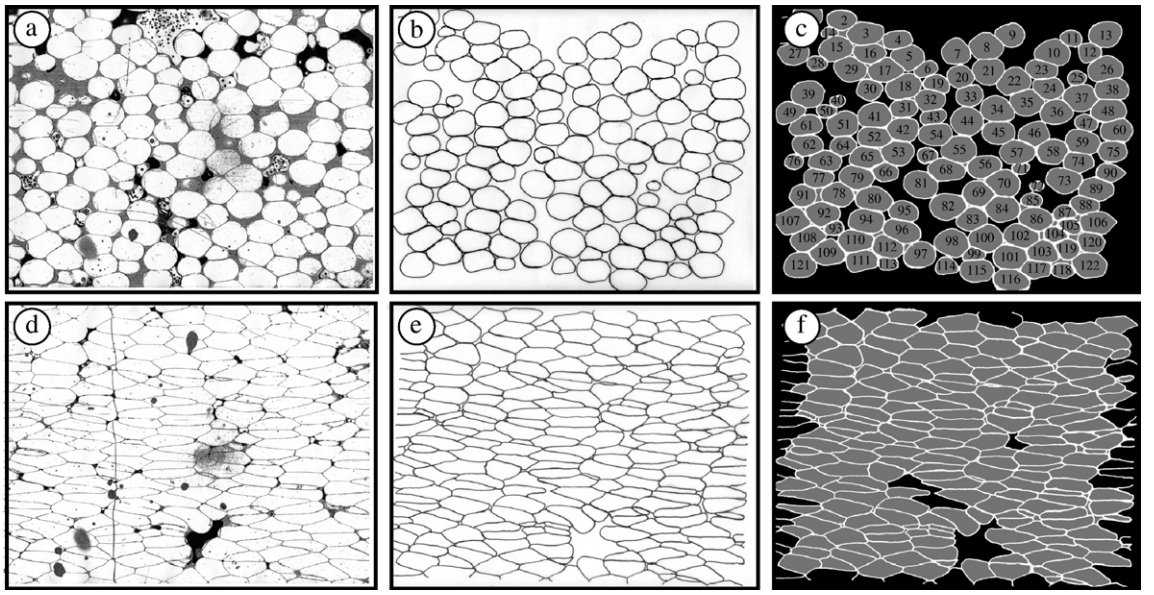

Fig. 4. Summary of steps in image analysis technique used to quantify particle shapes in experimental run products. Panels on left (a and d) represent microfiche images of a portion of sample thin sections. Middle panels (b and e) represent hand tracings of individual glass beads. Right panels (c and f) show analysis of center panel images to determine distribution of particle shapes. Black area represents void space and gray areas represent glass beads (individual beads numbered in c).

and f). The fit provided values of c and a for each particle.

3. Strain analysis

In this section, we use the revised values listed in Table 1 for initial porosity (ϕ_o), final porosity (ϕ_f), initial radius (r_o), final radius (r_f), sample displacement (ΔL), and individual glass bead particle elongation to analyze the nature and distribution of strain in the experimental run products.

3.1. Sample strain

The images of experimental run products shown in Fig. 2 help develop the strain model shown in Fig. 5. In our experiments, strain is accommodated in two distinct ways. Firstly, axial strain (ε_a) occurs where all of the strain (ΔL) is accommodated by porosity reduction and can be calculated from estimates of original (ϕ_o) and final (ϕ_f) porosity of the run product:

$$\varepsilon_a = \frac{\phi_o - \phi_f}{1 - \phi_f}. \quad (2)$$

During this deformation, the initial radius of the core (r_o) remains unchanged (Fig. 5b). Secondly, radial strain (ε_r) is accommodated by lateral bulging of the sample core due to viscous flow. Under these conditions porosity is preserved but the radius of the core increases with increasing strain (Fig. 5c); this component of strain is calculated as:

$$\varepsilon_r = 1 - \frac{r_o^2}{r_f^2} \quad (3)$$

where r_o is the radius of the core before experiment and r_f the mean radius of the run product (Quane et al., 2004; Quane and Russell, 2005a). The proportions or individual contributions of these styles of strain vary during the experiment and, thus, most experimental run products reflect a combination of the two end-members (Fig. 5d) and therefore the bulk strain (ε_b) in the sample is the sum of the independently measured values ε_a and ε_r. In many studies of viscous rheology, the experimental apparatuses are equipped with axial and radial strain gauges (e.g., Ducamp and Raj, 1989; Sura and Panda, 1990). Therefore, the relative amounts of strain accumulated by porosity reduction and by radius increase are determined directly from the experimental output (Ducamp and Raj, 1989; Sura and Panda, 1990). However, our device is not equipped with such strain gauges; therefore, we developed image analysis as an alternative means to quantify the relative proportions of axial and radial strain.

Machine strain (ε_m) is controlled during each experiment by the VDR (Quane et al., 2004). Therefore,

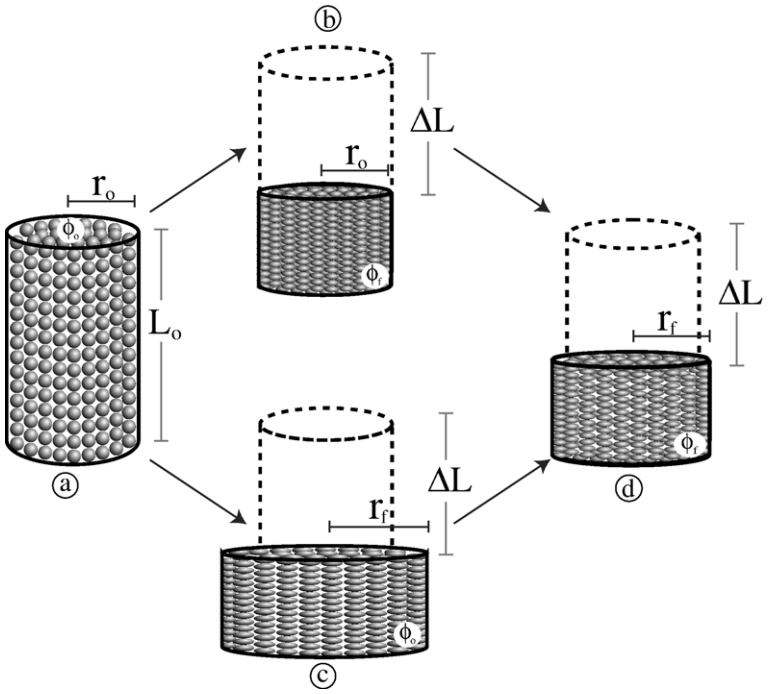

Fig. 5. Conceptual models for strain resulting from deformation experiments on glass bead cores. a) Starting material comprises cores of sintered spherical particles having an original length (L_o), radius (r_o) and porosity (ϕ_o), b) In the volume strain model, strain is manifest by shortening (ΔL) of the core and reduced porosity (ϕ_f) whereas the initial radius (r_o) is preserved. c) Pure shear strain conserves volume and, thus, is expressed by shortening of the core and an increase in the core's radius (r_f) but preserves porosity (ϕ_o). d) Deformed cores commonly record a combination of volume strain and pure shear strain expressed as shortening and bulging of the core and reduced porosity (ϕ_f).

after each experiment we know precisely how much piston displacement, or strain, the VDR has recorded. Sample strain (ε_s) is a measure of the amount of total strain accumulated within the entire sample. Sample strain is manifest many ways. One form of ε_s is the change in sample length (ΔL; Fig. 5). Generally, it is assumed that all instrumental strain (e.g., Fig. 1) is transferred to the sample. This is an important issue because if $\varepsilon_m \neq \varepsilon_s$, then interpretations of Fig. 1 become substantially more complicated. A prominent cause of $\varepsilon_m \neq \varepsilon_s$, is where strain is partitioned between the sample and the deformation apparatus (i.e., apparatus distortion is not corrected for; e.g., Tullis and Tullis, 1986; Austin et al., 2005) or if elastic strain is recovered after the load is released.

Results from image analysis of all 32 deformation experiments explored in this study are plotted in Fig. 6. Strain measured from machine output (ε_m) and from sample displacement (ε_s) plot on, or are dispersed evenly about, the line for 1 : 1 correlation (Fig. 6a). The good agreement between these measurements of strain indicates that all strain recorded by the deformation apparatus is being translated directly into the sample; no strain is being partitioned into the apparatus. We also compare ε_m to ε_b, the bulk strain represented by the sum of independently measured values of ε_a and ε_r. The machine strain is equal to the combined components of bulk sample strain (Fig. 6b), indicating that ε_m is being translated into the sample exclusively by porosity loss (ε_a) and/or by core radius increase (ε_r).

In this section, we demonstrated consistency between the amount of instrumental strain generated by the experimental apparatus (ε_m) and the actual strain transferred to the samples (ε_s). Furthermore, we subdivide ε_s into two components, ε_a and ε_r and show that there is also consistency between the total strain (instrumental or experimental) and the individual components of strain observed in the samples (Fig. 6).

The advantage of the methods employed here to determine ε_a and ε_r is that they are independent. For example, measurements of ϕ_f are made by using image analysis to directly measure porosity whereas measurements of r_f are achieved using measurements of core length and image analysis determinations of sample area. Because these measurements are independent, they more truly estimate the individual contributions of each strain component.

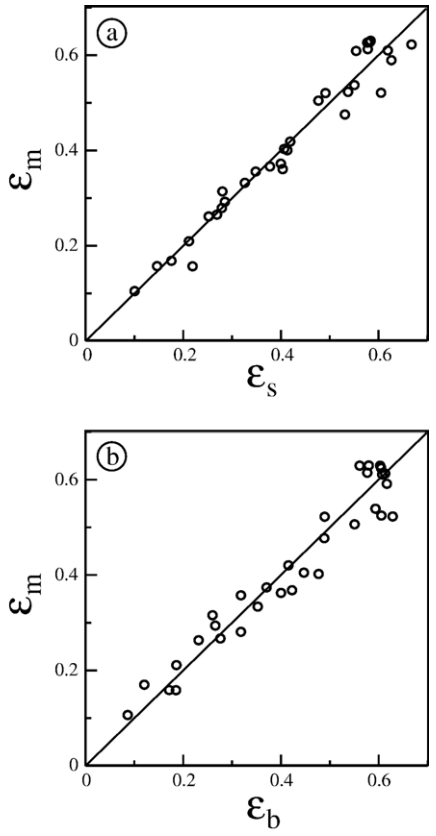

Fig. 6. Analysis of strain in high-T deformation experiments on soda-lime silica glass beads. a) Strain measured from machine displacement (ε_m) compared to strain measured from sample shortening (ε_s). Data are evenly distributed along 1 : 1 line for entire range of strains. b) Strain measured from machine displacement (ε_m) compared to the bulk strain (ε_b): the sum of axial (porosity loss) and radial (bulging) strain ($\varepsilon_a+\varepsilon_r$) as measured by image analysis. Data are also evenly distributed along 1 : 1 line for entire range of strains.

3.2. Particle strain

The individual solid particles within each core (e.g., glass beads) also record strain (Figs. 2 and 5). Glass beads are initially spherical (Fig. 2) but deform during the experiments. The strain recorded by these particles (e.g., particle strain; ε_p) provides an additional metric with which to track the evolution of strain throughout the experiment and to test or quantify how strain is being accommodated by the sample material. The glass beads are uniform in size so, when deformed under known conditions, each individual bead serves as a perfect strain marker. In the deformation experiments, glass beads deform to form flattened ellipsoids having equivalent equatorial axes of length a and b and polar axis c. When measured perpendicular to flattening direction, the height (c) and the length (a) of the beads fully describe the extent of deformation. Values of particle strain are obtained by determining the average c and a values in a population of particles and these values are used to determine an average ellipticity (Table 1) calculated using the equation:

$$\varepsilon_p = 1 - (c/a)^{2/3}. \quad (4)$$

Eq. (4) ensures that if all the strain imposed on the spherical glass beads is translated into pure shear, a 1 : 1 relationship will exist between ε_p and total strain (ε_m, ε_s or ε_b). Fig. 7 compares ε_p with ε_m. The data for each core fall on or are distributed evenly about a single line consistent with constant pure shear (Fig. 7). This relationship indicates that all strain recorded by the machine is partitioned into the sample and each particle evenly. If, for example, $\varepsilon_p < \varepsilon_m$ the beads might be rotating or rearranging to accommodate strain (i.e., reduce porosity) and not deforming viscously. Additionally, if $\varepsilon_p \neq \varepsilon_m$ some portion of the sample, not explored by image analysis, may have undergone strain localization or non-coaxial strain resulting in nonhomogenous distribution of strain in the sample. Furthermore, this indicates that the spherical beads accommodate strain by viscously flattening to form oblate spheroids and that there is no recoverable elastic strain in the samples. This is likely because the relaxation time-scale of the melt at these temperatures is short enough that stress does not build at point contacts between particles but, rather, is quickly dissipated by viscous flow.

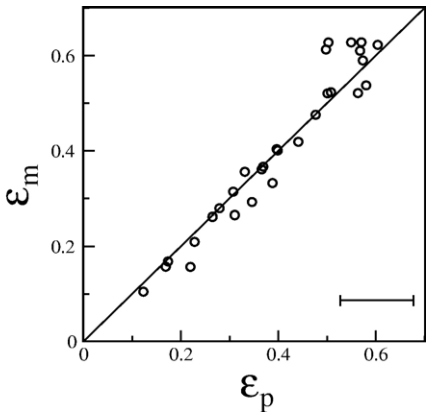

Fig. 7. Analysis of strain accommodation in high-T deformation experiments on glass beads. Estimates of particle strain (ε_p) from image analysis are plotted against strain recorded by machine displacement (ε_m). Data plot on or near solid line which is the theoretical relationship between particle deformation and strain for pure shear strain (see text for details). Bar in lower right corner is average uncertainty from Table 1.

4. Discussion

In the preceding sections, we showed how image analysis of experimental run products contributes to independent estimates of strain from: (a) shortening of samples (ε_s), (b) the sum of independently measured values of radial and axial deformation (ε_b) and (c) particle flattening (ε_p). In these experiments, all four metrics of strain agree ($\varepsilon_m = \varepsilon_s = \varepsilon_p = \varepsilon_b$; Figs. 6 and 7), which provides powerful corroboration of the internal consistency of the experimental output and the corresponding response of the sample cores.

Data from the deformation experiments on soda-lime silica glass bead cores at 600 °C and Rattlesnake Tuff rhyolite ash cores at 850 °C show very similar strain–time (constant load experiments) and stress–strain (constant displacement rate experiments) paths (Fig. 1). The only major difference in the experimental data is that the rhyolite ash cores require greater temperatures and stresses for deformation because of their higher viscosities (e.g., Quane, 2004; Quane and Russell, 2005a). By relying exclusively upon the experimental data, one might assume that the two materials were virtually identical in terms of rheology (Fig. 1). However, as demonstrated below, rheological models based solely on stress : strain : time datasets are vulnerable because they lack independent verification of the actual mechanisms of deformation.

Here, we investigate how strain is accommodated by the samples during the deformation experiments. Specifically, we compare how the proportions of radial and axial strain ($\varepsilon_r : \varepsilon_a$) vary with increasing strain (ε_m; Fig. 8). The two experimental data sets for cores of glass beads and rhyolitic ash show fundamental differences in how the different materials accumulate strain. In the cores of soda-lime silica beads, strain increases dominantly by porosity loss at low amounts of ε_m; however, as strain accumulates, the contribution of radial strain becomes increasingly important and begins to dominate at $>0.4\ \varepsilon_m$ (Fig. 8). In the cores of rhyolite ash the opposite trend is observed; radial bulging is dominant at lower amounts of ε_m and porosity loss becomes more and more important as ε_m increases (Fig. 8). This fundamental difference in strain accumulation between the two types of cores is most likely due to their physical characteristics. The soda-lime silica glass bead cores have relatively low initial porosity ($\phi_o = \sim 30\%$) when compared with the Rattlesnake Tuff ash cores ($\phi_o = \sim 73\%$). Furthermore, the soda-lime silica glass beads are originally solid and spherical whereas the Rattlesnake Tuff ash shards are porous and irregular. Therefore, natural glassy, particulate geomaterials at temperatures greater than their glass transition temperature (e.g., those undergoing welding) likely deform almost solely by porosity loss.

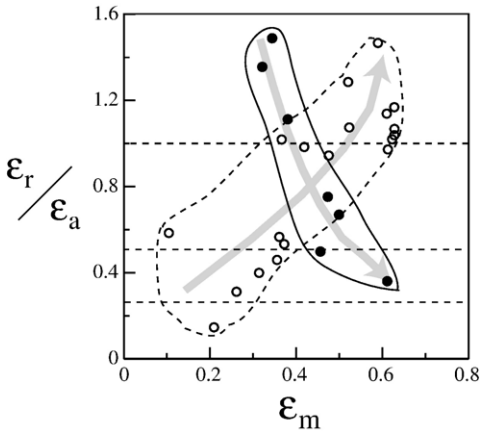

Fig. 8. Comparison of mechanisms of strain accumulation in soda-lime silica glass bead cores deformed at 600 °C (open circles) and Rattlesnake Tuff ash cores deformed at 850 °C (solid circles). The ratio of radial (ε_r) to axial (ε_a) stain is plotted versus machine strain (ε_m). Despite the similarities in experimental results shown in Fig. 1, strain is accommodated by these two different materials in drastically different ways (see text).

5. Conclusions

In this paper, we demonstrate the use and importance of image analysis techniques as an independent and objective means of mapping strain in samples deformed by high-temperature experiments. Post-experiment analysis of soda-lime silica glass bead and Rattlesnake Tuff rhyolite ash cores provides a wealth of textural and structural information which we have used to:

(a) verify coincidence between strain recorded by the experimental device and the total strain accumulated by the sample during the high-temperature deformation experiment,
(b) estimate porosity in post-experiment cores in order to compute axial strain,
(c) estimate the extent of bulging of post-experiment cores attributable to radial strain,
(d) evaluate the strain recorded by individual particles and, thereby, demonstrate coincidence between bulk strain of the sample and the strain recorded by the individual particles,
(e) demonstrate that strain was homogeneously distributed across the sample (e.g., no strain localization).

The experimental results summarized in Figs. 6, 7 and 8 demonstrate the importance of image analysis

measurements in determining a complete rheology for deformed geomaterials. Two materials with seemingly identical rheologies were shown to deform in quite different manners. Furthermore, the results pinpoint the limitations of soda-lime silica glass beads as an analogue material to describe the welding process. The glass beads were an excellent analogue material in terms of capturing the strain–time and stress–strain behavior of glassy, porous aggregates during deformation, but they did not fully capture the mechanisms of strain accumulation for natural pyroclastic materials.

Acknowledgements

The authors would like to thank J.V. Smith and Yan Lavallee for constructive reviews which led to positive changes in this manuscript. The Natural Sciences and Engineering Research Council of Canada (Discovery Grants program to JKR) and the Geological Society of America (Graduate Student Research Grant to SQ) supported this research.

References

Austin, N.J., Kennedy, L.A., Logan, J.M., Rodway, R., 2005. Textural controls on the brittle deformation of dolomite: the transition from brittle faulting to cataclastic flow. In: Gapais, D., Brun, J.P., Cobbold, P.R. (Eds.), Deformation Mechanisms, Rheology, and Tectonics: From Minerals to the Lithosphere, Geological Society of London, Special Publications, vol. 243, pp. 51–66.

Bagdassarov, N.S., Dingwell, D.B., Wilding, M.C., 1996. Rhyolite magma degassing: an experimental study of melt vesiculation. Bull. Volcanol. 57 (8), 587–601.

Bierwirth, P.N., 1982. Experimental welding of volcanic ash. Bachelors Thesis, Monash University.

Boyd, F.R., 1961. Welded tuffs and flows in the rhyolite plateau of Yellowstone Park, Wyoming. Geol. Soc. Am. Bull. 72, 387–426.

Chester, J.S., Lenz, S.C., Chester, F.M., Lang, R.A., 2004. Mechanisms of compaction of quartz sand at diagenetic conditions. Earth Planet. Sci. Lett. 220, 435–451.

Dingwell, D.B., 1998. Recent experimental progress in the physical description of silicic magma relevant to explosive volcanism. In: Gilbert, J.S., Sparks, R.S.J. (Eds.), The Physics of Explosive Volcanic Eruptions. Geol. Soc. Lond. Spec. Pub., vol. 145, pp. 9–26.

Ducamp, V.C., Raj, R., 1989. Shear and densification of glass powder compacts. J. Am. Ceram. Soc. 72, 798–804.

Friedman, I., Long, W., Smith, R.L., 1963. Viscosity and water content of rhyolite glass. J. Geophys. Res. 68, 6523–6535.

Giordano, D., Nichols, A.R.L., Dingwell, D.B., 2005. Glass transition temperatures of natural hydrous melts: a relationship with shear viscosity and implications for the welding process. J. Volcanol. Geotherm. Res. 142, 105–118.

Grunder, A.L., Laporte, D., Druitt, T.H., 2004. Experimental constraints on welding in rhyolitic ignimbrite. J. Volcanol. Geotherm. Res. 142, 89–104.

Guest, J.E., Rogers, T., 1967. The sintering of glass and its relationship to welding in ignimbrites. Proc. Geol. Soc. Lond. 1641, 174–177.

He, W., Hajash, D., Sparks, D., 2003. Creep compaction of quartz aggregates: effects of pore fluid—a combined experimental and theoretical study. Am. J. Sci. 303, 73–93.

Karato, S., Zhang, S., Zimmerman, M.E., Daines, M.J., Kohlstedt, D.L., 1998. Experimental studies of shear deformation of mantle materials; towards structural geology of the mantle. Pure Appl. Geophys. 151, 589–603.

Karner, S.L., Chester, F.M., Kronenberg, A.K., Chester, J.S., 2003. Subcritical compaction and yielding of granular quartz sand. Tectonophysics 377, 357–381.

Quane, S.L., 2004. Welding in pyroclastic deposits. PhD thesis, University of British Columbia. 208 pp.

Quane, S.L., Russell, J.K., 2005a. Welding: insights from high-temperature analogue experiments. J. Volcanol. Geotherm. Res. 142, 67–87.

Quane, S.L., Russell, J.K., 2005b. Ranking welding intensity in pyroclastic deposits. Bull. Volcanol. 67, 129–143.

Quane, S., Russell, J.K., Kennedy, L.A., 2004. A low-load, high-temperature deformation apparatus for volcanological studies. Am. Mineral. 89, 873–877.

Ross, C.S., Smith, R.L., 1961. Ash-flow tuffs their origin, geologic relations, and identification. U.S. Geol. Surv. Prof. Pap. 366 (81 pp.).

Russell, J.K., Quane, S.L., 2005. Rheology of welding: inversion of field constraints. J. Volcanol. Geotherm. Res. 142, 173–191.

Rutter, E.H., 1993. Experimental rock deformation: techniques, results and applications to tectonics. Geol. Today 9, 61–65.

Smith, R.L., 1960. Ash flows. Geol. Soc. Am. Bull. 71, 795–842.

Sparks, R.S.J., Wright, J.V., 1979. Welded air-fall tuffs. In: Chapin, C. E., Elston, W.E. (Eds.), Ash-Flow Tuffs. Special Paper Geol. Soc. Am. GSA, Boulder, CO, United States, pp. 155–166.

Spieler, O., Dingwell, D.B., Alidibirov, M., 2003. Magma fragmentation. J. Volcanol. Geotherm. Res. 129, 109–123.

Spieler, O., Kennedy, B., Kueppers, U., Dingwell, D.B., Scheu, B., Taddeucci, J., 2004. The fragmentation threshold of pyroclastic rocks. Earth Planet. Sci. Lett. 226 (1–2), 139–148.

Sura, V., Panda, P., 1990. Viscosity of porous glasses. J.Am. Ceram. Soc. 73, 2697–2701.

Tuffen, H., Dingwell, D.B., 2005. Fault textures in volcanic conduits: evidence for seismic trigger mechanisms during silicic eruptions. Bull. Volcanol. 67, 370–387.

Tullis, T.E., Tullis, J., 1986. Experimental rock deformation techniques. In: Hobbs, B.E., Heard, H.C. (Eds.), Mineral and Rock Deformation; Laboratory Studies; the Patterson Volume-Geophys. Mono., vol. 36, pp. 297–324.

Yagi, K., 1966. Experimental study on pumice and obsidian. Bull. Volcanol. 29, 559–572.